Ultrahigh Capacity Retention of Li_2ZrO_3-Coated Ni-rich LNCM811 Cathode Material through Covalent Interfacial Engineering

Zhangxian Chen,[†,‡,§] Qiuge Zhang,[†,§] Weijian Tang,[†,§] Zhaoguo Wu,[†,§] Juxuan Ding,[†,§] Cheng Huang,[†,§] Zeheng Yang,[*,†,§] Weixin Zhang[*,†,§1]

[†]School of Chemistry and Chemical Engineering, Hefei University of Technology, Hefei, Anhui 230009, P. R. China

[‡]School of Materials Science and Engineering, Hefei University of Technology, Hefei, Anhui 230009, P. R. China

[§]Anhui Key Laboratory of Controllable Chemical Reaction & Material Chemical Engineering, Hefei, Anhui 230009, P. R. China

[*] Corresponding authors.

Tel.: +86-551-62901450;

Fax: +86-551-62901450;

E-mails: zehengyang@hfut.edu.cn; wxzhang@hfut.edu.cn

[1] Weixin Zhang: ORCID 0000-0001-6979-8901

Abstract

Nickel-rich $LiNi_{0.8}Co_{0.1}Mn_{0.1}O_2$ (LNCM811) is a promising lithium-ion battery cathode material, whereas the surface-sensitive issues (i.e., side reaction and oxygen loss) occurring on LNCM811 particles significantly degrade their electrochemical capacity retentions. A uniform Li_2ZrO_3 coating layer can effectively mitigate the problem by preventing these issues. Instead of the normally used weak hydrogen-bonding interaction, we present a covalent interfacial engineering for the uniform Li_2ZrO_3 coating on $LiNi_{0.8}Co_{0.1}Mn_{0.1}O_2$ materials. Results indicate that the strong covalent interactions between citric acid and $Ni_{0.8}Co_{0.1}Mn_{0.1}(OH)_2$ precursor effectively promote the adsorption of ZrO_2 coating species on $Ni_{0.8}Co_{0.1}Mn_{0.1}(OH)_2$ precursor, which is eventually converted to uniform Li_2ZrO_3 coating layers of about 7 nm after thermal annealing. The uniform Li_2ZrO_3 coating endows LNCM811 cathode materials with an exceptionally high capacity retention of 98.7% after 300 cycles at 1 C. This work shows the great potential of covalent interfacial engineering for improving the electrochemical cycling capability of Ni-rich lithium-ion battery cathode materials.

Keywords: Lithium-ion battery; $LiNi_{0.8}Co_{0.1}Mn_{0.1}O_2$; Li_2ZrO_3 coating; Covalent interfacial engineering

1. Introduction

Nowadays, lithium-ion batteries (LIBs) have been widely used in various portable electronic devices, energy storage systems and electric vehicles (EVs), due to the relatively well-balanced performances, including high energy density and long cycle life.[1-5] The fast-growing EV market has set a higher standard for the specific capacity, cycle stability and thermal stability of LIBs. This places an essential requirement on cathode materials,[6,7] since the overall performances of a whole battery are primarily determined by cathode materials in current battery technology.

In a general formula of $Li[Ni_xCo_yMn_{1-x-y}]O_2$ (LNCM, $0<x+y<1$), the structure of layered lithium transition metal oxide cathode materialscan be regarded as a solid solution of $LiNiO_2$, $LiCoO_2$ and $LiMnO_2$.[8,9] Theoretical and experimental investigations have revealed that the capacity of LNCM is primarily contributed by $Ni^{2+/4+}$ and $Ni^{3+/4+}$ redox couples, while electrochemically inactive Mn^{4+} maintains the structural stability and Co^{3+} improves rate performance. Therefore, nickel-rich layered oxides ($LiNi_xCo_yMn_{1-x-y}O_2$, $x>0.5$) have aroused great research interest, not only due to their low cost and environmental friendliness, but also the high theoretical specific capacity (~270 $mAh \cdot g^{-1}$).[1,2,8-10]

However, a well-known issue of Li^+/Ni^{2+} cation mixing occurs throughout the whole LNCM cathode particles, especially as the nickel content is increased.[11,12] It is caused by the migration of Ni^{2+} from transition metal layer into Li^+ layer because of their similar ionic radii (r_{Li^+}=0.076 nm versus $r_{Ni^{2+}}$=0.069 nm). The issue can be greatly relieved by cationic or

anionic dopants that are capable of increasing the cation-anion bond strengths to prevent Ni^{2+} migration. In comparison, other key issues accompanying Ni-rich LNCM cathodes are more surface-sensitive.[13] Firstly, the high alkali residual content that leaves side products, such as LiOH, Li_2O, Li_2CO_3, on the particle surface,[14,15] would initiate side reactions during charging/ discharging processes. For example, lithium ions can be consumed by reaction with HF via the side reactions as following:

$LiPF_6 \rightarrow PF_5 + LiF\downarrow$

$H_2O + PF_5 \rightarrow POF_3 + 2HF$

$Li_2O + POF_3 \rightarrow Li_xPOF_y + LiF$

$Li_2O + 2HF \rightarrow H_2O + 2LiF$

Secondly, during repeated charging/discharging cycles, especially at a high cut-off charging voltage, cathode particle surface undergoes a slow release of oxygen.[16] This would turn the surface from layered phase into an electrochemically inert NiO-like phase via an intermediate spinel phase. Thirdly, the dissolution of transition metal gradually occurs from cathode particles into electrolyte through the particle/electrolyte interface, due to the attack by side products, such as HF.[17] Lastly, highly reactive species (i.e., Ni^{4+} and atomic oxygen), formed on the particle surface during charging process, would cause side reactions with electrolytes or organic solvents.[18] These issues collectively cause deteriorations in the electrochemical performances of Ni-rich LNCM cathodes, including lowered rate capability, reduced capacity and decayed cycling life.

Li_2ZrO_3 coating is considered as an effective approach to improve the electrochemical performance of Ni-rich cathode materials. The coating layer can prevent the air-sensitive

surface of Ni-rich $LiNi_xCo_yMn_{1-x-y}O_2$ cathode particles from formation of side products, such as Li_2CO_3. More importantly, the coating layer can stabilize the cathode particles by inhibiting oxygen loss, metal dissolution and Ni^{4+}-induced side reactions occurring at the cathode/electrolyte interfaces.[19] The Li_2ZrO_3 coating on cathode materials was commonly accomplished by the hydrolysis of Zr-containing inorganic salts (i.e., $Zr(NO_3)_4$, $ZrO(NO_3)_2$) or alkoxides (i.e., $Zr(OC_3H_7)_4$, $Zr(OC_4H_9)_4$).[20-23] Although their fast hydrolysis rates were commonly controlled by using non-aqueous solvents, including ethanol and propanol,[20-22] the hydrolyzed products are not preferably bonded to the surface of the cathode (or cathode precursor) particles due to the weak interactions (i.e., hydrogen bonding) between the hydrolyzed Zr-containing species (i.e., hydrated ZrO_2) and cathode particles. Therefore, drying of the hydrolyzed coating solutions is essentially required to prevent the loss of hydrolyzed Zr-containing species during the repeated washing steps.[20-23] Thus, a stronger interaction between the hydrolyzed Zr-containing precursor and Ni-rich LNCM cathode materials is highly necessary to achieve effective coating of Li_2ZrO_3.

Herein, we present a covalent interfacial engineering for uniformly Li_2ZrO_3-coated nickel-rich $LiNi_{0.8}Co_{0.1}Mn_{0.1}O_2$ (LNCM811) cathode materials, which employs citric acid molecules for the pretreatment of $Ni_{0.8}Co_{0.1}Mn_{0.1}(OH)_2$ precursor. Due to the strong covalent bonding between citric acid and transition metal sites, the Zr-containing coating species can be firmly captured on the $Ni_{0.8}Co_{0.1}Mn_{0.1}(OH)_2$ precursor particles. Eventually, uniform Li_2ZrO_3 coating layer on the Ni-rich $LiNi_{0.8}Co_{0.1}Mn_{0.1}O_2$ cathode materials is achieved after thermal annealing. Density functional theory simulations confirm that the adsorption of ZrO_2 cluster on cathode precursor can be greatly enhanced by using the covalent interfacial

engineering. The uniform Li_2ZrO_3 coating significantly improves the cycling performance of $LiNi_{0.8}Co_{0.1}Mn_{0.1}O_2$ nickel-rich cathode materials. In addition, the high thermal energy drives the partial diffusion of Zr^{4+} from surface into the bulk to form concentration-gradient Zr^{4+} doping. The stronger Zr-O bonds also helps to inhibit the Li^+/Ni^{2+} cation mixing and cooperatively improve the electrochemical cycling performances and thermal stabilities of $LiNi_{0.8}Co_{0.1}Mn_{0.1}O_2$ cathode materials.

2. Experiments and theoretical calculations

All the reagents were in analytical grade and directly used without further purification.

2.1 Preparation of NCM811 precursor

The $Ni_{0.8}Co_{0.1}Mn_{0.1}(OH)_2$ (NCM811) precursor was prepared using a co-precipitation method, according to our previous report.[24,25] In detail, 1.8 L of mixed sulfate solution ($NiSO_4/CoSO_4/MnSO_4$=8/1/1 in molar ratio; 2 M in total metal concentration) and 0.54 L of ammonia solution (5 M) were injected into a 5-L continuous-stirring tank reactor (CSTR) using peristaltic pumps, under N_2 atmosphere at 60 °C. The pH value of the reaction system was adjusted to be 10.5 by controlling the feed rate of NaOH solution (10 M). After 12 h of reaction, the precipitate was collected by repeated washing with deionized water and ethanol, and finally drying in vacuum at 120 °C.

2.2 Covalent Interfacial Engineering for Li_2ZrO_3 coating

Typically, 1 g of NCM811 precursor and 0.5 g citric acid were dispersed in 100 mL of water-ethylene glycol mixture (volume ratio=1:1) at room temperature under constant stirring. After 3 h, the solid was collected after washing by deionized water and ethanol to remove excess citric acid. The sample is denoted as CA-treated NCM811.

To perform Li_2ZrO_3 coating, the CA-treated NCM811 samples were dispersed in three separate solutions (50 mL) containing 0.035 g, 0.070 g and 0.140 g of $ZrOCl_2 \cdot 8H_2O$, respectively. The pH value of the solution was adjusted to 5.0 by 0.1 M urea solution (50 mL) to promote the formation of hydrolyzed Zr-containing species. The mixtures were continuously stirred at 85 °C for 6 h. The powders collected after washing and drying were mixed with Li_2CO_3 (5% excess) by manual grinding. The mixed powders were preheated at 450 °C for 5 h and calcined at 750 °C for 15 h. The final Li_2ZrO_3-coated $LiNi_{0.8}Co_{0.1}Mn_{0.1}O_2$ products prepared with 0.035 g, 0.070 g and 0.140 g of $ZrOCl_2 \cdot 8H_2O$ are marked as LNCM811-Zr1, LNCM811-Zr2 and LNCM811-Zr3, respectively. The $LiNi_{0.8}Co_{0.1}Mn_{0.1}O_2$ sample without Li_2ZrO_3 coating is recorded as LNCM811-Zr0.

2.3 Characterization

The phase composition and lattice parameter of the prepared products were analyzed on a X'Pert PRO MPD power X-ray diffraction (XRD) instrument with Cu K_α radiation (λ=0.154178 nm). The morphology, elemental mapping and energy dispersive spectra (EDS) were characterized on a SU8020 field emission scanning electron microscopy (FESEM). High-resolution transmission electron microscopy (HRTEM) was analyzed on a JEM-2100F microscope. X-ray photoelectron spectroscopy (XPS) was performed on an ESCALAB250Xi instrument. Thermal stability of the cathode materials was analyzed by a STA449F3 differential scanning calorimetry (DSC), from room temperature to 800 °C with a heating rate of 10 °C·min^{-1}.

2.4 Electrochemical testing

The cathode was prepared by casting the slurry containing active material (80 wt%),

Super-P conductive carbon black (10 wt%) and polyvinylidene fluoride (PVDF, 10 wt%) in N-methyl-2-pyrrolidone (NMP) onto Al foils. The wet cathode was then dried at 80 °C for 12 h in vacuum. CR2032 coin cells were assembled in an Ar-filled glove box, with Li foil and 1.0 M $LiPF_6$ in ethylene carbonate/dimethyl carbonate mixed solvent (volume ratio=1/3) as the anode and electrolyte, respectively. Electrochemical performances of the cathode materials were evaluated at 25 °C using NEWARE instrument under the voltage between 2.8 V and 4.3 V (vs. Li^+/Li). Cyclic voltammetry (CV) was carried out at the scanning speeds within 0.1~0.6 mV s^{-1}.

2.5 Density functional theory calculations

Periodic density functional theory calculations were conducted using the VASP code.[26] The electron-ion interactions were described by the projector augmented wave method (PAW).[27] The electron exchange-correlation functional was represented by the Perdew-Burke-Ernzerhof (PBE) functional.[28] A cutoff energy of 540 eV was used throughout the computations. The structures were fully optimized until the total energy and force converged to 10^{-5} eV and 0.01 eV/Å, respectively.

A simplified β-$Ni(OH)_2$ (001) surface was used to represent the $Ni_{0.8}Co_{0.1}Mn_{0.1}(OH)_2$ precursor surface, which shows the lowest surface energy among all low-index facets.[29] The $Ni(OH)_2$ (001) surface consists of a 4×4 supercell along *a* and *b* axes. A vacuum of 20 Å was inserted to prevent the artificial interactions along *c* axis, leading to a slab size of 12.708×12.708×29.202 $Å^3$. A ZrO_2 cluster was used to qualitatively compare the bonding interactions between the hydrolyzed Zr-containing coating species and the $Ni_{0.8}Co_{0.1}Mn_{0.1}(OH)_2$ precursor particles. The *k*-point mesh (3×3×1) was sampled using the

Monkhorst-Pack method.[30] The adsorption energy (E_{ads}) is calculated as:

$$E_{ads}=E_{surf}+E_{ZrO2}-E_{surf\text{-}ZrO2}$$

E_{surf} and E_{ZrO2} refer to the total energies of optimized $Ni(OH)_2$ (001) surface and ZrO_2 cluster, respectively. $E_{surf\text{-}ZrO2}$ denote the total energy of the surface with adsorbed ZrO_2.

3. Results and discussion

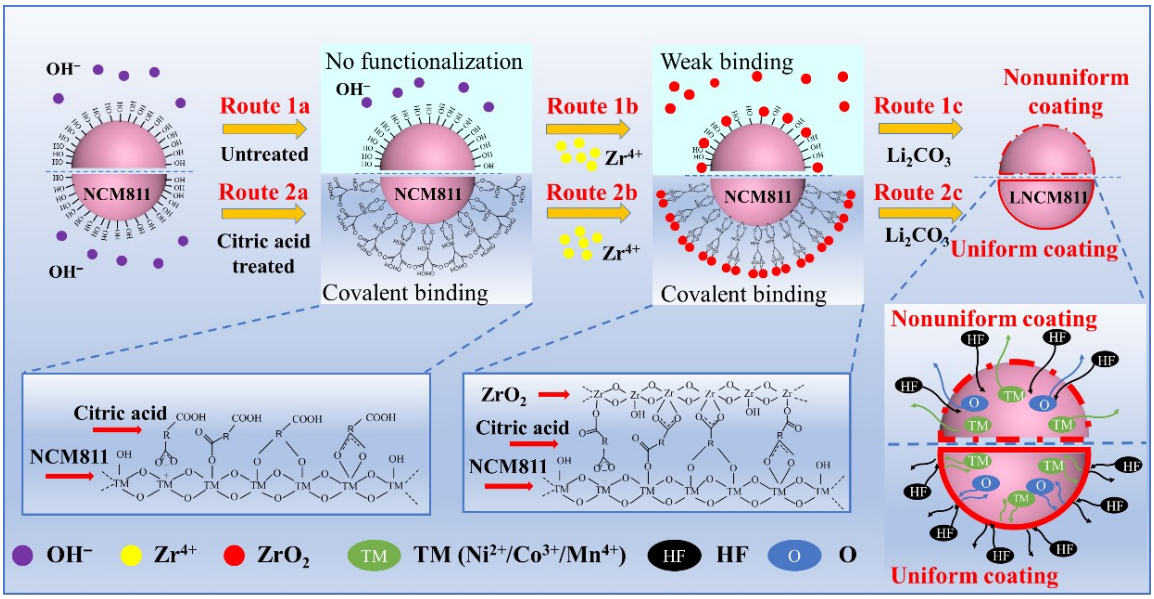

FIGURE 1 Schematic illustration of the covalent interfacial engineering for Li_2ZrO_3 coating on LNCM811 cathode material

Our covalent interfacial engineering can be illustrated by Figure 1. The $Ni_{0.8}Co_{0.1}Mn_{0.1}(OH)_2$ (NCM811) precursor particles are full of hydroxyl groups. The commonly used surface modification methods do not employ any covalent interfacial engineering (Route 1a). The adsorption of hydrolyzed ZrO_2 coating species (through the hydrolysis of $ZrOCl_2$ in our case) on NCM811 particles is not preferred due to their weak hydrogen bonding interaction (Route 1b). Therefore, this would finally lead to non-uniform Li_2ZrO_3 coating on $LiNi_{0.8}Co_{0.1}Mn_{0.1}O_2$ cathode particles (Route 1c), leaving the core active

$LiNi_{0.8}Co_{0.1}Mn_{0.1}O_2$ (LNCM811) materials vulnerable to the attack by side products (such as HF) and dissolution of transition metals, etc. In contrast, the covalent interfacial engineering through the reaction between citric acid and NCM811 would functionalize the particles by citric acid molecules (Route 2a). As demonstrated below, citric acid molecules would facilely attach on the NCM811 particle surface via various strong covalent interactions, such as monodentate and bidentate bindings, to form carboxylate-like species. The adsorbed citric acid molecules can further serve as the interfacial linker to firmly capture the hydrolyzed ZrO_2 coating species (Route 2b). The covalent interfacial engineering greatly promotes the coating of hydrolyzed Zr-containing species on NCM811 particles, finally leading to uniform Li_2ZrO_3 coating on $LiNi_{0.8}Co_{0.1}Mn_{0.1}O_2$ cathode particles (Route 2c). The uniform coating layer can effectively protect the core active materials from the above-mentioned surface-sensitive issues, such as side reactions and oxygen loss.

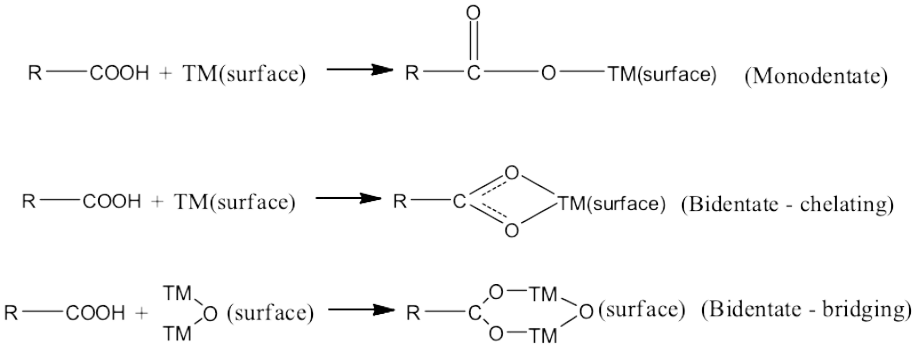

IR and Raman spectroscopies have been used to identify the different reaction intermediates. Obviously, the pristine $Ni_{0.8}Co_{0.1}Mn_{0.1}(OH)_2$ particles show a sharp and typical O-H stretching band at about 3620 cm^{-1} (Sample NCM811 in Figure 2a), due to the metal-hydroxide chemical nature of NCM811 precursor. By comparing the FTIR spectra, we can easily identify two new bands at around 1402 and 1567 cm^{-1} for citric acid-treated NCM811

(Sample NCM811/CA in Figure 2a). The two new peaks represent the typical symmetric (ν_s) and asymmetric (ν_{as}) stretching modes of carboxylate, respectively.[31,32] The absorption feature is also significantly different from that of pure citric acid (Sample CA in Figure 2a), suggesting the successful CA-treatment of NCM811 precursor.

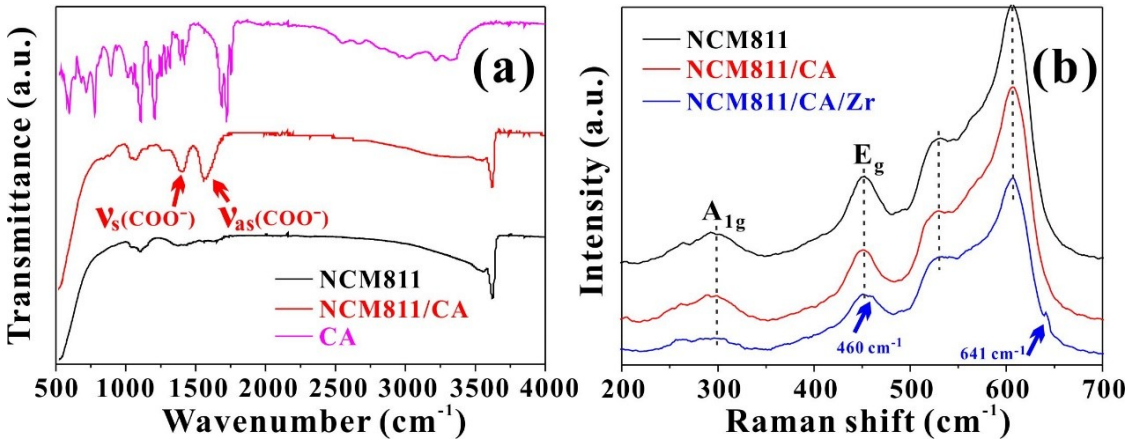

FIGURE 2 (a) FTIR and (b) Raman spectra of pure citric acid and NCM811 with different treatments. (NCM811/CA refers to NCM811 sample treated only with citric acid. NCM811/CA/Zr refer to the sample treated sequentially by citric acid and Zr-containing coating.)

The Raman spectrum of NCM811 precursor (Sample NCM811 in Figure 2b) shows two peaks at about 300 and 451 cm^{-1}, corresponding to the typical translational A_{1g} and E_g modes of β-$Ni(OH)_2$, respectively.[33] The co-precipitation of Co^{2+} is responsible for the Raman band at about 525 cm^{-1}.[33] The strong peak at about 606 cm^{-1} is probably due to the vibration of Mn-O bonds.[34] By comparing the Raman spectra of NCM811 sample with citric acid (Sample NCM811/CA in Figure 2b) and further with ZrO_2 coating (Sample NCM811/CA/Zr), we can observe two new peaks centering at about 641 and 460 cm^{-1} (Marked with blue arrows), respectively, corresponding to monoclinic phase of ZrO_2.[35] The weak intensity of ZrO_2 is

understandable, because the peak positions are overlapping with those of NCM811 and the coating layer is rather thin (several nanometers) on the final cathode particles, as will be discussed below.

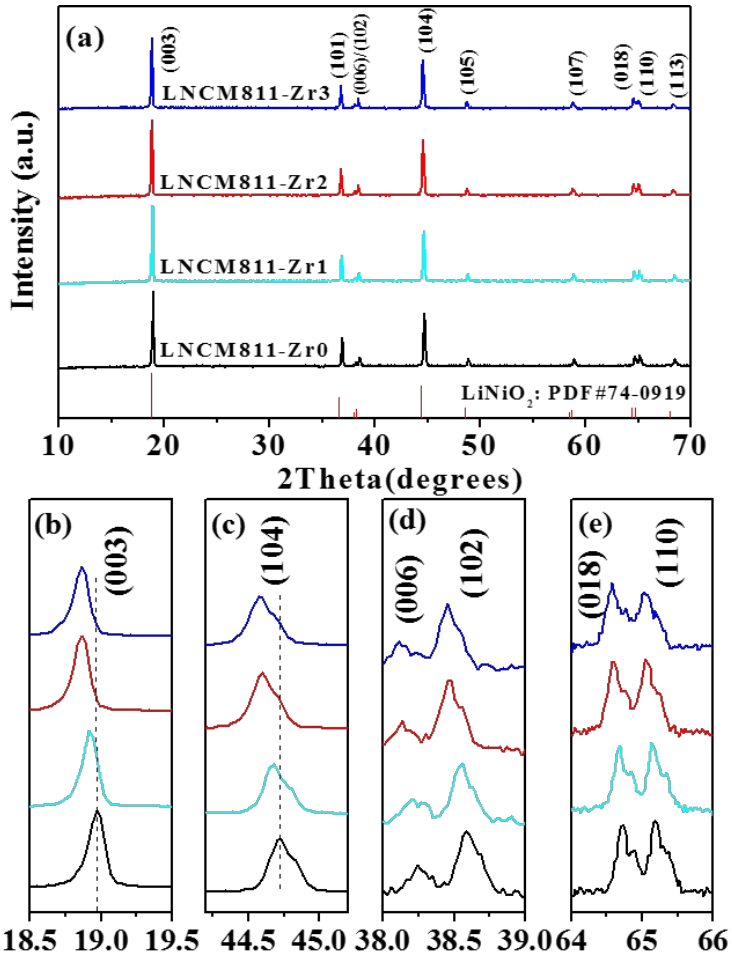

FIGURE 3 (a) XRD patterns of the pristine and Li_2ZrO_3-coated LNCM811 samples. (b-e) Enlarged diffraction peak position comparisons for the LNCM811 samples. Vertical line in (a) shows the standard pattern of $LiNiO_2$ (PDF #74-0919)

The XRD pattern of LNCM811 without Li_2ZrO_3 coating (LNCM811-Zr0) can be indexed to the $R\bar{3}m$ layered $LiNiO_2$ structure, in consistence with the standard pattern (PDF#74-0919) (Figure 3a). After the LNCM811 samples coated with different amounts of Li_2ZrO_3, no

obvious impurity peaks can be observed. The clear splitting of (006)/(102) and (018)/(110) diffraction peaks can be observed, suggesting the well-defined layered hexagonal structure for all samples (Figure 3d-e). The cation mixing induced by the migration of Ni^{2+} into Li^{+} layer would reduce the diffraction interference of (003) plane and increase the interference of (104) plane. Thus, the degree of Li^{+}/Ni^{2+} cation mixing can be evaluated by the intensity ratio of the two Miller planes. A larger value of $I_{(003)}/I_{(104)}$ suggests less cation mixing. Obviously, the intensity ratios for all the LNCM811 samples are larger than 1.2 (Table 1), implying their low degree of Li^{+}/Ni^{2+} cation mixing.[36] The specific crystal structures of all samples were further analyzed. The corresponding lattice parameters show that the c/a ratios for all LNCM811 samples are larger than 4.9, implying that the synthesized LNCM811 samples possess ordered layered structure,[37] especially the LNCM811-Zr2 sample with the best layered order.

TABLE 1 Lattice parameters of the pristine and Li_2ZrO_3-coated LNCM811 samples. $I_{(003)}/I_{(104)}$ refers to the intensity ratio of (003) and (104) Miller planes

Samples	**$I_{(003)}/I_{(104)}$**	**a (Å)**	**c (Å)**	**c/a**
LNCM811-Zr0	1.3438	2.8766	14.2327	4.9478
LNCM811-Zr1	1.4140	2.8685	14.2132	4.9549
LNCM811-Zr2	1.4244	2.8684	14.2512	4.9683
LNCM811-Zr3	1.3485	2.8748	14.2173	4.9454

Figure 3b-e compare the 2θ positions for (003), (104), (006)/(102) and (018)/(110)

Miller planes, respectively. It should be noted that the (003) and (104) diffraction peaks shift to a lower angle after Li_2ZrO_3 coating, suggesting their increasing lattice parameters. During the high-temperature calcination process, $Ni_{0.8}Co_{0.1}Mn_{0.1}(OH)_2$ particles are converted to $LiNi_{0.8}Co_{0.1}Mn_{0.1}O_2$. Meanwhile, a small portion of Zr^{4+} cations slowly diffuses into the lattice of inner particles and occupies the transition metal site.[38] The ionic radius of Zr^{4+} is 72 pm, bigger than those of Ni^{2+}, Co^{3+} and Mn^{4+} ($r_{Ni^{2+}}$=69 pm, $r_{Co^{3+}}$=68 pm, $r_{Mn^{4+}}$=53 pm).[11] The incorporated larger-size Zr^{4+} cations thus expand the lattice volumes. A series of EDS point scans along radial direction of a broken LNCM811-Zr2 particle indicate that the ratio of Zr element is gradually reduced from surface into the core (Figure S1 in Supporting Information). This strongly suggests the synergistic concentration-gradient Zr^{4+} doping after Li_2ZrO_3 coating.[39]

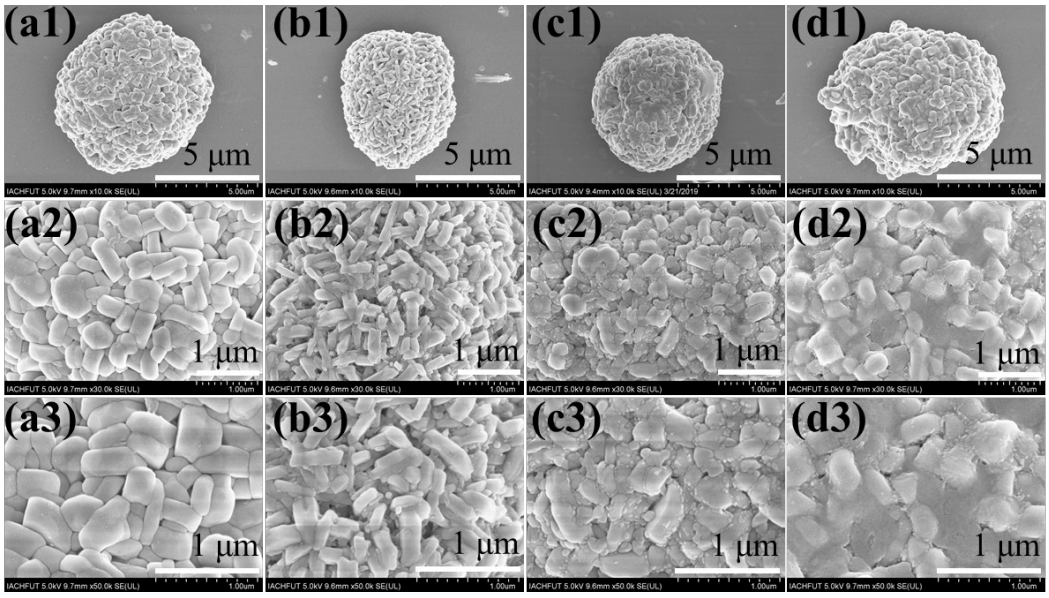

FIGURE 4 FESEM images of the pristine and Li_2ZrO_3-coated LNCM811 samples; (a) LNCM811-Zr0; (b) LNCM811-Zr1; (c) LNCM811-Zr2; (d) LNCM811-Zr3. From top to

bottom, the magnification is increased

The Li_2ZrO_3-coated LNCM811 particles (Figure 4b-d) do not show obvious morphological changes with the pristine sample (Figure 4a). Only LNCM811-Zr3 sample with a high coating amount shows a slight difference that the voids among the primary particles are filled (Figure 4d). ICP-MS has been used to detect the ratios of each metal element in the samples (Table S1) and the Ni: Co: Mn ratios are in good agreement with the nominal ratio of 8:1:1. The Li_2ZrO_3 coating amounts of LNCM811-Zr1, LNCM811-Zr2 and LNCM811-Zr3 are determined to be 0.4 wt%, 1.17 wt% and 1.29 wt%, respectively.

LNCM811-Zr2 sample has the best electrochemical performances (discussed later) and has been chosen as a typical sample to demonstrate the microstructural changes of the cathode materials after Li_2ZrO_3 coating. As presented in Figure 5a, a uniform coating layer can be distinguished on the particle surface, which suggests the successful coating of Ni-rich layered cathode materials with the current method. Each element including Ni, Co, Mn and O is also uniformly distributed in the particle (Figure 5b). The visual contrast on Zr elemental mapping is relatively weaker than others, which results from the thin surface coating layer compared with the core cathode material, as proven by the ICP-MS results (Table S1). Another reason is the partial doping of Zr^{4+} into the particles, as discussed in Figure S1. TEM image shows the uniform coating layer with the thickness of about 7 nm on the surface of LNCM811-Zr2 particle (Figure 5c), which is more homogeneous than the sample prepared without the covalent interfacial engineering by citric acid (Figure S2).

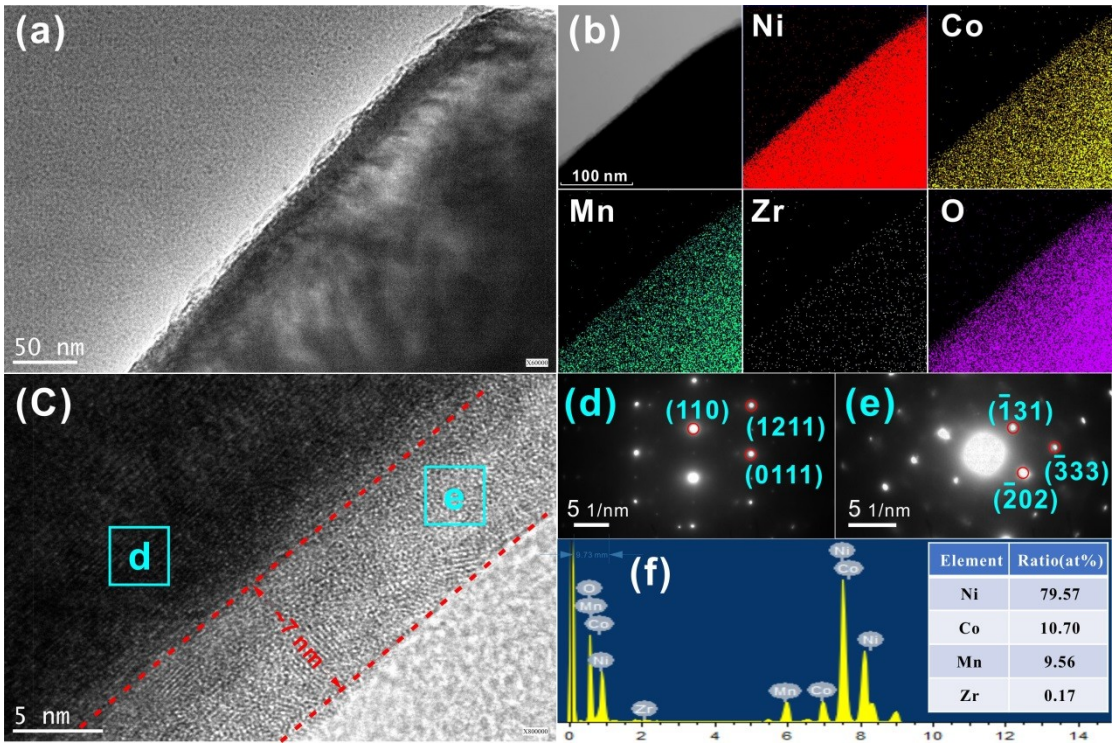

FIGURE 5 Microstructural characterizations of sample LNCM811-Zr2: (a) TEM image, (b) elemental mappings, (c) HRTEM image, (d-e) electron diffraction patterns and (f) EDS spectrum. The electron diffractions correspond to the core and surface region as labeled in (c)

The electron diffraction pattern of the cathode core (Figure 5d) shows the (1 1 0) and (0 1 11) planes of typical $R\bar{3}m$ phase $LiNi_{0.8}Co_{0.1}Mn_{0.1}O_2$, whereas the coating layer (Figure 5e) presents the $(\bar{1}\ 3\ 1)$ and $(\bar{2}\ 0\ 2)$ diffraction planes of monoclinic phase of Li_2ZrO_3. The formation of lithium zirconate can further be supported by XRD pattern of the cathode with more coatings (i.e., 5 wt%), in which we can clearly differentiate the respective peaks from cathode and the coating layer (Figure S3 in Supporting Information). The EDS spectrum further supports the coating ratio and nominal compositions of each metal element (Figure 5f).

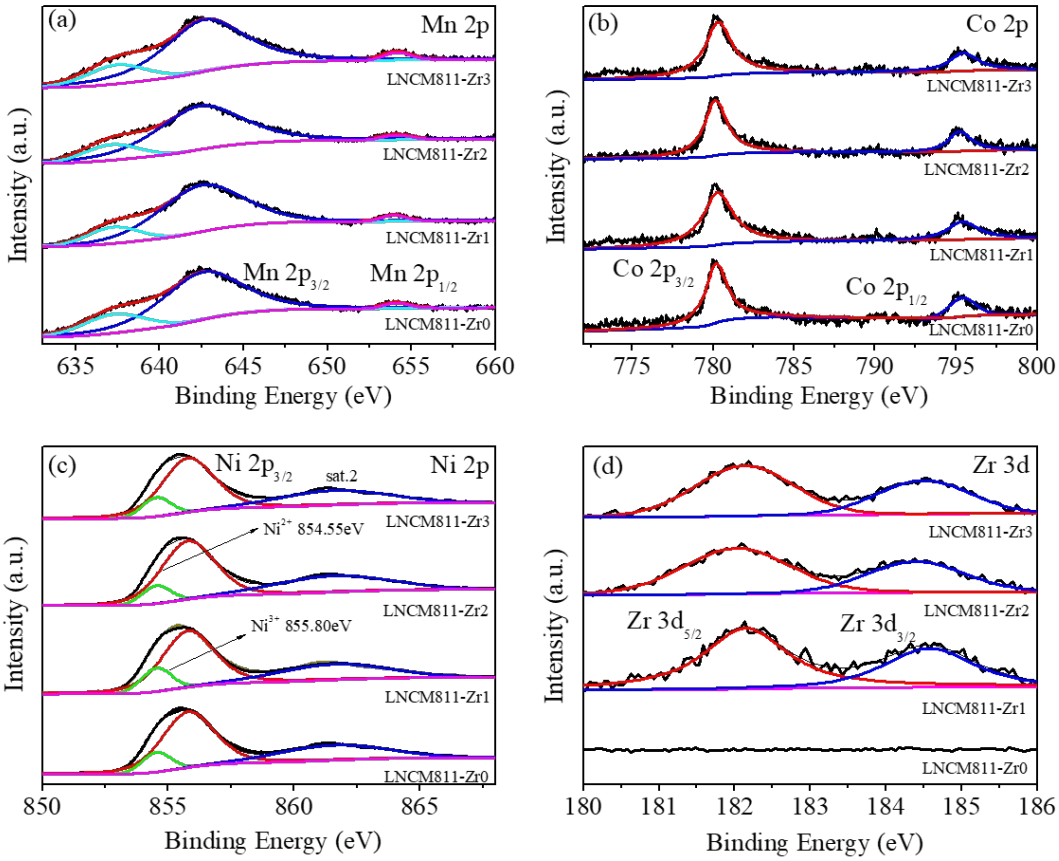

FIGURE 6 (a) Mn 2p, (b) Co 2p, (c) Ni 2p, and (d) Zr 3d core-level XPS spectra of the pristine and Li_2ZrO_3-coated LNCM811 samples

XPS was used to investigate the surface chemical state of the pristine and Li_2ZrO_3-coated samples. The binding energies of Mn $2p_{3/2}$ and Co $2p_{3/2}$ peak are located at 642.4 and 780.0 eV (Figure 6a-b), respectively, suggesting that the valence states of Mn and Co are +4 and +3, respectively. The Li_2ZrO_3 coating does not cause obvious variation in peak positions. The Ni $2p_{3/2}$ peaks can be fitted into two peaks (Figure 6c), with one centered at the binding energy of 855.80 eV and the other at 854.55 eV, corresponding to Ni^{3+} and Ni^{2+}, respectively.[40] Furthermore, we have noted that the proportion of Ni^{3+} is increased after Li_2ZrO_3 coating. As tabulated in Table S2, the highest ratio of Ni^{3+} can be found in LNCM-Zr2 sample, implying its lowest cation mixing. A sharp contrast can be observed in Zr 3d

core-level XPS peak for the pristine and Li_2ZrO_3-coated LNCM811 samples (Figure 6d). Obviously, no Zr 3d peak can be found for the pristine LNCM811 sample. After Li_2ZrO_3 coating, Zr $3d_{3/2}$ and $3d_{5/2}$ peaks appear at 182.1 and 184.4 eV, respectively, corresponding to typical Zr^{4+} chemical state in Li_2ZrO_3.[38] This strongly supports the formation of Li_2ZrO_3 coating layer on the Ni-rich cathode materials.

The electrochemical performances of Li_2ZrO_3-coated LNCM811 cathode materials were thoroughly investigated. Figure 7a shows the initial charge-discharge curves of pristine and Li_2ZrO_3-coated cathode materials at 0.5 C. The initial coulomb efficiency for LNCM-Zr2 is79.0%, superior to the pristine LNCM811 material. Figures 7b-c compare the CV curves of the LNCM811-Zr0 and LNCM811-Zr2 samples tested at a sweep speed 0.1 mV/s for 5 cycles. Obviously, both CV curves show two pairs of redox peaks around 3.9/3.7 V and 4.3/4.2 V, respectively. The oxidation peak of sample LNCM811-Zr2 appears at 3.86 V in the first cycle and stabilizes at 3.79 V in the next few cycles, whereas its reduction peak remains at 3.67 V (Figure 7b). Similar trend can be observed for sample LNCM811-Zr0, which is due to the first-cycle activation of the cathode materials (Figure 7c). This redox pair is related to the electrochemical oxidations of Ni^{2+}/Ni^{3+} to Ni^{4+}, occurring with the transformation from hexagonal (H) to monoclinic (M) phase.

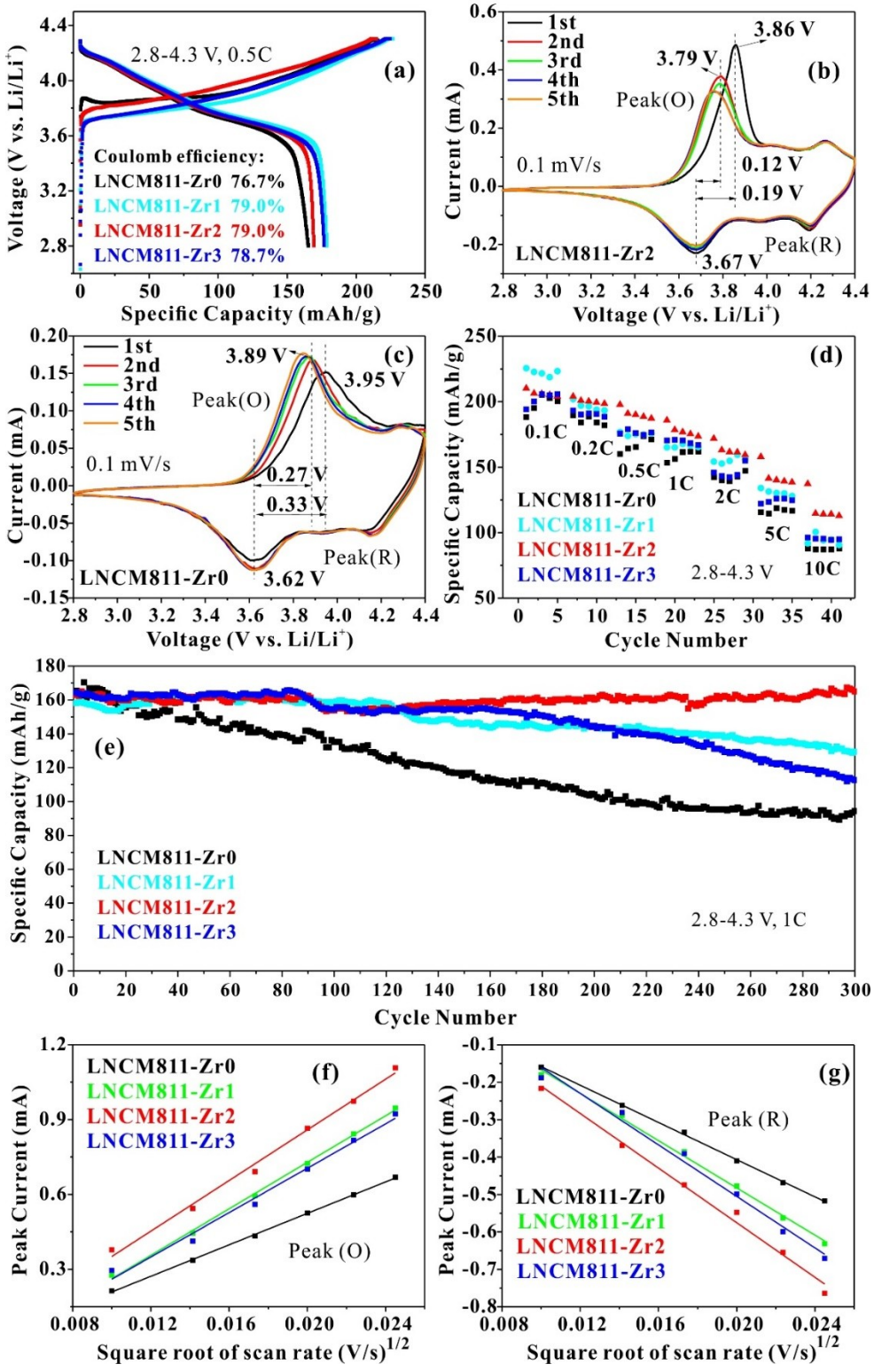

FIGURE 7 (a) The first-cycle charge and discharge curves for the LNCM811 samples. The first five-cycle CV curves for (b) LNCM811-Zr2 and (c) LNCM811-Zr0. (d) The rate and (e) performances for the LNCM811 samples. Peak current fittings by (f) oxidative peaks and (g)

reductive peaks

The other redox pair at 4.3/4.2 V suggests the electrochemical oxidation of Co^{3+} to Co^{4+} during charging state, corresponding H2 to H3 phase change.[24,41] The CV curves indicate that less polarization exist after the cathode material is coated by Li_2ZrO_3, which is beneficial for the improvement of rate and cycling capabilities. Indeed, the discharge capacities of LNCM811 cathodes can be greatly improved after Li_2ZrO_3 coating, especially when the current density is increased from 0.5 to 10 C (Figure 7d).

Figure 7e compares the discharge cycling performances of pristine and Li_2ZrO_3-coated samples within 2.8~4.3 V. The pristine LNCM811-Zr0 sample exhibits an initial discharge capacity of 165.3 $mAh \cdot g^{-1}$ at a high current density of 1 C, whereas LNCM811-Zr1, LNCM811-Zr2 and LNCM811-Zr3 show the discharge capacities of 158.2, 165.1 and 164.4 $mAh \cdot g^{-1}$, respectively. The first-cycle discharge capacities of the Li_2ZrO_3-coated samples are slightly reduced, due to the inert Li_2ZrO_3 coating layer that cannot provide discharge capacity. As tabulated in Table S3, the capacity for the pristine LNCM811-Zr0 sample fades quickly to 94.4 $mAh \cdot g^{-1}$ after 300 cycles, corresponding to a capacity retention of only 57.1%. In contrast, the cycle stability can be greatly improved after Li_2ZrO_3 coating. The LNCM811-Zr1, LNCM811-Zr2 and LNCM811-Zr3 samples exhibit the significantly enhanced capacity retentions of 81.8%, 98.7% and 68.2%, respectively after 300 cycles (Table S3). As compared in Table S4, the capacity retention of 98.7% after 300 cycles at the current rate of 1 C for LNCM811-Zr2 is superior to the recently reported pristine or coated LNCM811 cathode materials. The improved electrochemical performances should be attributed to the greatly enhanced crystal structure and electrode/electrolyte stabilities, as revealed by the reduced Li^+/

Ni^{2+} cation mixing and uniform coating layer obtained by XRD and SEM. The coating layer is helpful to reduce the corrosion in cathode material by the side products (such as HF) and the dissolution of active transition metals. The charge-discharge curves at different cycle numbers under 1 C of further suggests that the Li_2ZrO_3 coating is helpful to improve the electrochemical reversibility of LNCM811 cathode materials (Figure S4a-d).

The potential difference of redox peaks (ΔE) is a useful indication of the electrochemical reversibility and polarization degree of the electrode materials. By increasing the scanning rate from 0.1 to 0.6 mV/s, ΔE becomes larger. This is commonly observed if the electrochemical reaction is diffusion controlled.[42] For diffusion-controlled reversible electrochemical reaction, the peak current (I_p) of the redox peaks can be described by the Randles-Sevcik equation,[42] as following:

$$I_p=2.69\times10^5\times n^{3/2}\times A\times D^{1/2}\times \nu^{1/2}\times C_0$$

Here n, A, C_0, D and ν denote the number of transferred electrons, the electrode area, the Li^+ concentration, the Li^+ diffusion coefficient and the scan rate in cyclic voltammetry. Except D and ν, other parameters can be approximately regarded as a constant. Therefore, by a linear fitting of I_p versus $\nu^{1/2}$, we can get the lithium diffusion coefficient in the electrode materials. As displayed in Figure 7f, the peak current is in good linear relationship with $\nu^{1/2}$. The Li_2ZrO_3-coated samples have larger slops of linear fitting, implying that Li^+ diffusion is more favorable in the Li_2ZrO_3-coated LNCM811 samples. Especially, the sample LNCM811-Zr2 has the largest slope. All cathode samples show the Li^+ diffusion coefficient on the order of 10^{-11} cm^2 s^{-1} (Table 2). LNCM811-Zr2 sample has the highest of 4.10×10^{-11} cm^2 s^{-1}, more than twice that of the pristine cathode sample. The fitting of reduction peaks and the

corresponding Li-extraction diffusion coefficient exhibit the similar trend (Figure 7g), supporting the improvement of Li^+ diffusion through the $LiNi_{0.8}Co_{0.1}Mn_{0.1}O_2$ by Li_2ZrO_3 coating.

TABLE 2 Calculated lithium-ion diffusion coefficients for pristine and Li_2ZrO_3-coated samples

Samples	D_{Li^+} ($cm^2\ s^{-1}$) (Li-insertion)	D_{Li^+} ($cm^2\ s^{-1}$) (Li-extraction)
LNCM811-Zr0	1.90×10^{-11}	3.06×10^{-11}
LNCM811-Zr1	3.07×10^{-11}	6.69×10^{-11}
LNCM811-Zr2	4.10×10^{-11}	7.94×10^{-11}
LNCM811-Zr3	3.64×10^{-11}	6.10×10^{-11}

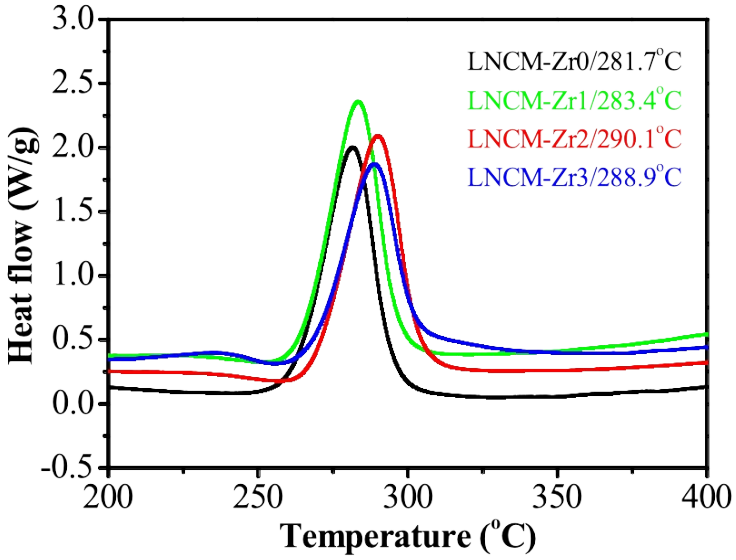

FIGURE 8 DSC profiles of the pristine and Li_2ZrO_3-coated samples

Thermal runaway caused by the release of active oxygen from the Ni-rich LNCM811 cathode materials is a major safety problem that prevents their application. The problem could be more serious when the battery is cycled at a higher temperature. To compare the thermal stability of the pristine and Li_2ZrO_3-coated samples, we used differential scanning

calorimetry (DSC) to analyze the thermal behaviors of pristine and Li_2ZrO_3-coated samples. As presented in Figure 8, the exothermic peak for the pristine LNCM811 material is located at 281.7 °C and the Li_2ZrO_3 coating can shift the peaks to a higher temperature. Especially, sample LNCM811-Zr2 has a greatly enhanced peak temperature at 290.1 °C, indicating the improved thermal stability of Ni-rich LNCM811 sample after Li_2ZrO_3 coating.

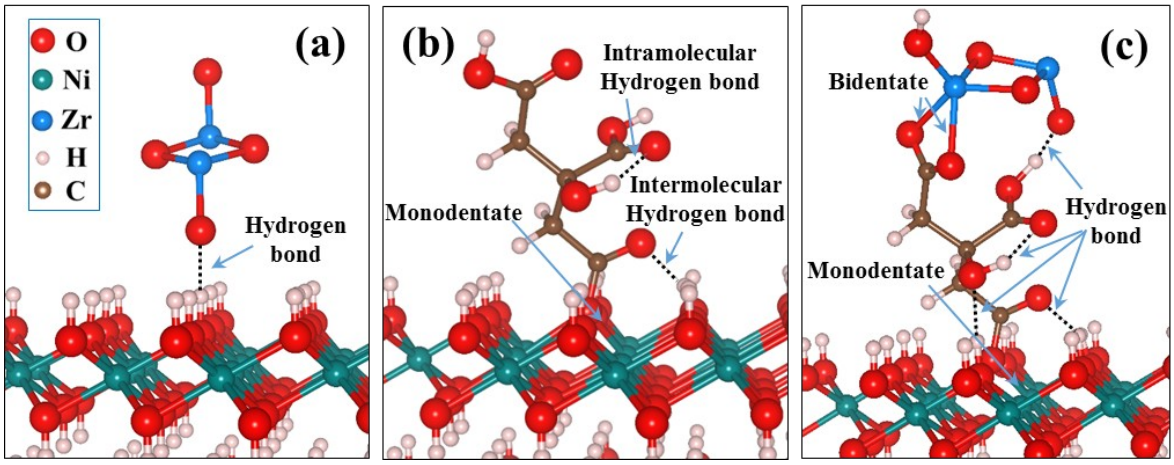

FIGURE 9 The optimized structures of (a) ZrO_2 cluster adsorbed on clean $Ni(OH)_2$ (001) surface and (b) citric acid adsorbed on $Ni(OH)_2$ (001) surface. (c) The optimized structure of ZrO_2 cluster adsorbed on $Ni(OH)_2$ (001) surface via covalent interfacial engineering. Hydrogen bonds are shown in dashed lines

To further support the experimental results, DFT calculations have been performed to compare the bonding interaction between the hydrolyzed Zr-containing coating species and NCM811 surface. The $Ni_{0.8}Co_{0.1}Mn_{0.1}(OH)_2$ particles adopts the hexagonal phase β-$Ni(OH)_2$ structure (XRD shown in Figure S5a), whose (001) facet has the lowest surface energy.[29] Therefore, the simplified β-$Ni(OH)_2$ (001) surface was used to represent the NCM811 surface (Optimized structure shown in Figure S5b). Figure 9a shows that ZrO_2 cluster prefers to be adsorbed on $Ni(OH)_2$ (001) surface via hydrogen bonding. The adsorption is rather weak, as

implied by its low adsorption energy of 0.69 eV (Table 3). In contrast, the adsorption of citric acid molecule occurs via the monodentate binding mode as well as an intermolecular hydrogen bonding between citric acid and surface OH group (Figure 9b). The adsorption is much stronger as revealed by the significantly high adsorption energy of 3.29 eV (Table 3). The adsorption of ZrO_2 cluster on the citric acid-pretreated $Ni(OH)_2$ (001) surface is even stronger. As presented in Figure 9b, the dissociation of exposed carboxyl group leads to the bidentate binding of ZrO_2 cluster. An additional intermolecular hydrogen bonding between ZrO_2 cluster and citric acid molecule further strengthens the adsorption by increasing the adsorption energy to 3.99 eV (Table 3). The DFT calculations confirm that the anchoring of hydrolyzed Zr-containing coating species can be effectively improved on the citric acid-treated $Ni_{0.8}Co_{0.1}Mn_{0.1}(OH)_2$ particles via significantly stronger covalent interactions. The results well explain the effectiveness of the covalent interfacial engineering strategy for uniform Li_2ZrO_3 coating to improve the electrochemical cycling capability of LNCM811 cathode materials.

TABLE 3 The calculated adsorption energies of different adsorbates on $Ni(OH)_2$ (001) surface

Adsorbate	**ZrO_2**	**Citric acid**	**Citric acid/ZrO_2**
Adsorption Energy (eV)	0.69	3.29	3.99

4. Conclusions

In summary, we have presented a covalent interfacial engineering for the uniform Li_2ZrO_3 coating on $LiNi_{0.8}Co_{0.1}Mn_{0.1}O_2$ cathode materials. DFT calculation and experimental results reveal that citric acid can strongly promote the adsorption of hydrolyzed ZrO_2 on cathode precursor, due to the strong covalent interactions, including monodentate and

bidentate bonding. This eventually gives rise to the uniform Li_2ZrO_3 coating layer on the $LiNi_{0.8}Co_{0.1}Mn_{0.1}O_2$ Ni-rich cathode materials. The uniform Li_2ZrO_3 coating layer effectively inhibit the formation of residual alkali on cathode materials and protect the active materials from the transition metal dissolution and oxygen loss. Detrimental side reactions induced by such as HF attack and Ni^{4+} oxidation of solvents would also be greatly prevented due to the uniform Li_2ZrO_3 coating layer. The Li_2ZrO_3-coated $LiNi_{0.8}Co_{0.1}Mn_{0.1}O_2$ cathode materials show superior capacity retention compared with the bare $LiNi_{0.8}Co_{0.1}Mn_{0.1}O_2$ cathode. For example, the LNCM811-Zr2 sample exhibits an exceptionally high capacity retention of 98.71% after 300 cycles at a high current rate of 1 C, significantly higher than that of 57.10% for the pristine $LiNi_{0.8}Co_{0.1}Mn_{0.1}O_2$. The diffusion coefficient of Li-insertion is 4.10×10^{-11} cm^2 s^{-1}, more than twice that of the pristine sample. Due to the effective stabilization of the cathode/electrolyte interface achieved by the current covalent interfacial engineering, the Li_2ZrO_3-coated cathode materials also display greatly enhanced thermal stability. This work shows the great potential of the covalent interfacial engineering for the improvement of capacity retention of Ni-rich layered cathode materials.

AUTHOR INFORMATION

Corresponding Authors

E-mail: zehengyang@hfut.edu.cn (Z. H. Yang).

E-mail: wxzhang@hfut.edu.cn (W. X. Zhang).

Notes

The authors declare no competing financial interest.

Acknowledgments

We greatly appreciate the financial supports from National Natural Science Foundation of China (NSFC Grants 91834301 and 91534102), the Special Fund for Key Program of Science and Technology of Anhui Province (202003a05020046 and 201903a05020021), the Fundamental Research Fund for the Central University (JZ2018YYPY0299).

References

1. Bi YJ, Tao JH, Wu YQ, Li LZ, Xu YB, Hu EY, Wu BB, Hu JT, Wang CM, Zhang JG, Qi Y, Xiao J. Reversible planar gliding and microcracking in a single-crystalline Ni-rich cathode. *Science***.** 2020;370:1313-1317.
2. Kim Y-H, Park G-T, Son B-K, Nam GW, Liu J, Kuo LY, Kaghazchi P, Yoon CS, Sun Y-K. Heuristic solution for achieving long-term cycle stability for Ni-rich layered cathodes at full depth of discharge. *Nat. Energy*. 2020;5:860-869.
3. Chen ZX, Zhang WX, Yang ZH. A review on cathode materials for advanced lithium ion batteries: microstructure designs and performance regulations. *Nanotechnology*. 2020;31:012001.
4. Tang WJ, Chen ZX, Huang HJ, Irfan M, Huang C, Yang ZH, Zhang WX. PVP-bridged γ-$LiAlO_2$ nanolayer on $Li_{1.2}Ni_{0.182}Co_{0.08}Mn_{0.538}O_2$ cathode materials for improving the rate capability and cycling stability, *Chem. Eng. Sci.* 2021;229:116126.
5. Deng ZN, Jiang H, Hu YJ, Li CZ, Liu Y, Liu HL. Nanospace-confined synthesis of coconut-like SnS/C nanospheres for high-rate and stable lithium-ion batteries. *AIChE J.* 2018;64:1965-1974.
6. Zhang XF, Lengyel M, Axelbaum RL. Nanostructured high-energy $x$$Li_2MnO_3$·(1-$x$)$LiNi_{0.5}Mn_{0.5}O_2$ ($0.3 \leq x \leq 0.6$) cathode materials. *AIChE J.* 2014;60:443-450.

7. Winter M, Barnett B, Xu K. Before Li Ion Batteries. *Chem. Rev.* 2018;118:11433-11456.

8. Manthiram A, Song B, Li W. A Perspective on Nickel-rich Layered Oxide Cathodes for Lithium-ion Batteries. *Energy Storage Mater.* 2017;6:125-139.

9. Lee W, Muhammad S, Kim T, Kim H, Lee E, Jeong M, Son S, Ryou J-H, Yoon W-S. New Insight into Ni-Rich Layered Structure for Next-Generation Li Rechargeable Batteries. *Adv. Energy Mater.* 2018;8:1701788.

10. Manthiram A, Knight JC, Myung ST, Oh SM, Sun YK. Nickel-Rich and Lithium-Rich Layered Oxide Cathodes: Progress and Perspectives. *Adv. Energy Mater.* 2016;6:1501010.

11. Kim H, Kim MG, Jeong HY, Nam H, Cho J. A New Coating Method for Alleviating Surface Degradation of $LiNi_{0.6}Co_{0.2}Mn_{0.2}O_2$ Cathode Material: Nanoscale Surface Treatment of Primary Particles. *Nano Lett.* 2015;15:2111-2119.

12. Sun G, Yin X, Yang W, Song A, Jia C, Yang W, Du Q, Ma Z, Shao G. The Effect of Cation Mixing Controlled by Thermal Treatment Duration on the Electrochemical Stability of Lithium Transition-metal Oxides. *Phys. Chem. Chem. Phys.* 2017;19:29886-29894.

13. Etacheri V, Marom R, Elazari R, Salitra G, Aurbach D. Challenges in the Development of Advanced Li-ion Batteries: A Review. *Energy Environ. Sci.* 2011;4:3243-3262.

14. Li J, Manthiram A. A Comprehensive Analysis of the Interphasial and Structural Evolution over Long-Term Cycling of Ultrahigh-Nickel Cathodes in Lithium-Ion Batteries. *Adv. Energy Mater.* 2019;9:1902731.

15. Aurbach D. Electrode-solution Interactions in Li-ion batteries: a Short Summary and New Insights. *J. Power Sources*. 2003;119-121:497-503.

16. Xu J, Hu E, Nordlund D, Mehta A, Ehrlich SN, Yang XQ, Tong W. Understanding the Degradation Mechanism of Lithium Nickel Oxide Cathodes for Li-Ion Batteries. *ACS Appl. Mater. Interfaces*. 2016;8:31677-31683.

17. Zhan C, Wu T, Lu J, Amine K. Dissolution, Migration, and Deposition of Transition Metal Ions in Li-ion Batteries Exemplified by Mn-based Cathodes-a Critical Review. *Energy Environ. Sci.* 2018;11:243-257.

18. Hwang S, Chang W, Kim SM, Su D, Kim DH, Lee JY, Chung KY, Stach EA. Investigation of Changes in the Surface Structure of $Li_xNi_{0.8}Co_{0.15}Al_{0.05}O_2$ Cathode Materials Induced by the Initial Charge. *Chem. Mater.* 2014;26:1084-1092.

19. Sari HMK, Li X. Controllable Cathode-Electrolyte Interface of $Li[Ni_{0.8}Co_{0.1}Mn_{0.1}]O_2$ for Lithium Ion Batteries: A Review. *Adv. Energy Mater.* 2019;9:1901597.

20. Zhang YQ, Tian Y, Xiao Y, Miara LJ, Aihara Y, Tsujimura T, Shi T, Scott MC, Ceder G. Direct Visualization of the Interfacial Degradation of Cathode Coatings in Solid State Batteries: A Combined Experimental and Computational Study. *Adv. Energy Mater.* 2020;10:1903778.

21. Zhan X, Gao S, Cheng Y-T. Influence of annealing atmosphere on Li_2ZrO_3-coated $LiNi_{0.6}Co_{0.2}Mn_{0.2}O_2$ and its high-voltage cycling performance. *Electrochim. Acta*. 2019;300:36-44.

22. Song B, Li W, Oh S-M, Manthiram A. Long-Life Nickel-Rich Layered Oxide Cathodes with a Uniform Li_2ZrO_3 Surface Coating for Lithium-Ion Batteries. *ACS Appl. Mater. Interfaces*. 2017;9:9718-9725.

23. Zhai Y, Yang W, Ning D, Yang J, Sun L, Schuck G, Schumacher G, Liu X. Improving the

cycling and air-storage stability of $LiNi_{0.8}Co_{0.1}Mn_{0.1}O_2$ through integrated surface/interface/doping engineering. *J. Mater. Chem. A*. 2020;8:5234-5245.

24. Tang WJ, Chen ZX, Xiong F, Chen F, Huang C, Gao Q, Wang TZ, Yang ZH, Zhang WX. An Effective Etching-induced Coating Strategy to Shield $LiNi_{0.8}Co_{0.1}Mn_{0.1}O_2$ Electrode Materials by $LiAlO_2$. *J. Power Sources*. 2019;412:246-254.
25. Xiong F, Chen ZX, Huang C, Wang TZ, Zhang WX, Yang ZH. Near-Equilibrium Control of Li_2TiO_3 Nanoscale Layer Coated on $LiNi_{0.8}Co_{0.1}Mn_{0.1}O_2$ Cathode Materials for Enhanced Electrochemical Performance. *Inorg. Chem.* 2019;58:15498-15506.
26. Kresse G, Furthmüller J. Efficient iterative schemes for ab initio total-energy calculations using a plane-wave basis set. *Phys. Rev. B*. 1996;54:11169-11186.
27. Blöchl PE. Projector augmented-wave method. *Phys. Rev. B*. 1994;50:17953-17979.
28. Perdew JP, Burke K, Ernzerhof M. Generalized Gradient Approximation Made Simple. *Phys. Rev. Lett.* 1996;77:3865-3868.
29. Tkalych AJ, Yu K, Carter EA. Structural and Electronic Features of β-$Ni(OH)_2$ and β-NiOOH from First Principles. *J. Phys. Chem. C*. 2015;119:24315−24322.
30. Monkhorst HJ, Pack JD. Special points for Brillouin-zone integrations. *Phys. Rev. B*. 1976;13:5188-5192.
31. Pujari SP, Scheres L, Marcelis AT, Zuilhof H. Covalent surface modification of oxide surfaces. *Angew. Chem. Int. Ed.* 2014;53:6322-6356.
32. Miller FA. Amides, Carboxylate Ion, and C-O Single Bonds. In: Course Notes on the Interpretation of Infrared and Raman Spectra; John Wiley & Sons, Inc.: New York, 2004; 205-215.
33. Audemer A, Delahaye A, Farhi R, Sac-Epée N, Tarascon JM. Electrochemical and Raman

Studies of Beta-Type Nickel Hydroxides $Ni_{1-x}Co_x(OH)_2$ Electrode Materials. *J. Electrochem. Soc.* 1997;144:2614-2620.

34. Gostzola D, Weaver MJ. Electroinduced structural changes in manganese dioxide+manganese hydroxide films as characterized by real-time surface-enhanced Raman spectroscopy. *J. Electroanal. Chem.* 1989;271:141-154.
35. Zaki MI, Ali AAM. A surface study of zirconia-based solid acids by Laser Raman spectroscopy of adsorbed pyridine. *Colloids Surf. A*. 1996;119:39-50.
36. Min K, Kim K, Jung C, Seo S-W, Song YY, Lee HS, Shin J, Cho E. A comparative study of structural changes in lithium nickel cobalt manganese oxide as a function of Ni content during delithiation process. *J. Power Sources.* 2016;315;111-119.
37. Liu W, Oh P, Liu X, Lee M-J, Cho W, Chae S, Kim Y, Cho J. Nickel-Rich Layered Lithium Transition-Metal Oxide for High-Energy Lithium-Ion Batteries. Angew. Chem. Int. Ed.2015;54;4440-4457.
38. He T, Lu Y, Su Y, Bao L, Tan J, Chen L, Zhang Q, Li W, Chen S, Wu F. Sufficient Utilization of Zirconium Ions to Improve the Structure and Surface properties of Nickel-Rich Cathode Materials for Lithium-Ion Batteries. *ChemSusChem*. 2018;11:1639-1648.
39. Sivaprakash S, Majumder SB. Understanding the Role of Zr^{4+} Cation in Improving the Cycleability of $LiNi_{0.8}Co_{0.15}Zr_{0.05}O_2$ Cathodes for Li Ion Rechargeable Batteries. *J. Alloys Compd.* 2009;479:561-568.
40. Liang L, Sun X, Wu C, Hou L, Sun J, Zhang X, Yuan C. Nasicon-Type Surface Functional Modification in Core-Shell $LiNi_{0.5}Mn_{0.3}Co_{0.2}O_2$@$NaTi_2(PO_4)_3$ Cathode Enhances Its High-Voltage Cycling Stability and Rate Capacity toward Li-Ion Batteries.

ACS Appl. Mater. Interfaces, 2018;10:5498-5510.

41. Wu F, Liu N, Chen L, Su Y, Tan G, Bao L, Zhang Q, Lu Y, Wang J, Chen S, Tan J. Improving the Reversibility of the H2-H3 Phase Transitions for Layered Ni-rich Oxide Cathode Towards Retarded Structural Transition and Enhanced Cycle Stability. *Nano Energy*. 2019;59:50-57.
42. Liu W, Li X, Xiong D, Hao Y, Li J, Kou H, Yan B, Li D, Lu S, Koo A, Adair K, Sun X. Significantly Improving Cycling Performance of Cathodes in Lithium Ion Batteries: The Effect of Al_2O_3 and $LiAlO_2$ Coatings on $LiNi_{0.6}Co_{0.2}Mn_{0.2}O_2$. *Nano Energy*. 2018;44:111-120.